BULLETIN OF THE POLISH ACADEMY OF SCIENCES
TECHNICAL SCIENCES,
DOI: 10.24425/bpasts.2026.1950

Trajectory generation with complex no-fly zone constraints for hypersonic morphing vehicle

Yong LI[1,2], Hui LI[1], Lixin WANG[2], Luhua LIU[3*]

[1] China Special Vehicle Research Institute, Jingmen 448035, China
[2] School of Aeronautic Science and Engineering, Beihang University, Beijing 100191, China
[3] School of Aeronautics and Astronautics, Sun Yat-sen University, Shenzhen 518107, China

Abstract. This paper investigates the flight capability and trajectory generation of hypersonic morphing vehicles under complex no-fly zone constraints. A target flight path containing only position information is constructed and discretized based on the characteristics of the complex no-fly zone. An optimization model for the control variables is formulated, and an iterative stepping strategy along with a no-fly zone avoidance strategy is designed to develop a tracking algorithm for the target flight path. The trajectory generation algorithm for complex no-fly zone constraints is then completed. The reachable domain under no-fly zone constraints and the applicability of the proposed algorithms are analyzed using both a hypersonic morphing vehicle model and a hypersonic fixed-wing vehicle model. Simulation results demonstrate that the hypersonic morphing vehicle can utilize the proposed trajectory generation algorithm to design a feasible trajectory that complies with the complex no-fly zone constraints. Compared with the hypersonic fixed-wing vehicle, the hypersonic morphing vehicle exhibits a larger reachable domain under no-fly zone constraints and demonstrates a stronger capability for avoiding complex no-fly zone constraints.

Key words: hypersonic vehicle; morphing vehicle; complex no-fly zone; trajectory generation

1. INTRODUCTION

Hypersonic morphing vehicles feature broad operational envelopes and exceptional maneuverability, with rapid technological advances highlighting their immense potential for both military and civilian applications. Optimal trajectory generation is a pivotal research topic for these vehicles, yet the intricate constraints and increased optimization variables pose significant challenges [1, 2].

Recent progress in hypersonic trajectory generation has been driven by pseudo-spectral methods [3, 4], convex optimization [5, 6], and artificial intelligence [7, 8], alongside studies addressing flight environment and model uncertainties [9, 10, 11]. For morphing vehicles specifically, Rudnick-Cohen *et al.* [12, 13] integrated trajectory and configuration optimization, while Cai and Wang [14, 15] employed convex optimization and reinforcement learning to tackle high dimensionality and convergence difficulties. Despite these advances, generating trajectories under no-fly zone constraints remains a formidable challenge.

No-fly zones arise from threat avoidance or geopolitical restrictions. While numerical algorithms like pseudo-spectral [16, 17] and convex optimization [18, 19] have addressed typical no-fly zone avoidance, they often incur lengthy computation and require segmented optimization. Real-world no-fly zone constraints are complex, involving multiple circular [20] and dynamic no-fly zones [21]. Virtual waypoint methods offer a promising alternative: He *et al.* [22] select waypoints on a minimum-cost 2D path, while Zhang *et al.* [23, 24] employ graph theory and depth search. However, these methods neglect the vehicle's flight state, requiring post-hoc feasibility checks. A more integrated strategy designs a geometric path to avoid no-fly zones and tracks it to complete the avoidance maneuver, with the key challenge being accurate path tracking under all vehicle constraints. Mature results exist for hypersonic landing [25, 26], though specialized geometric paths are cumbersome and hard to extend. Recent efforts have combined geometric paths with dynamic modeling[27, 28, 29]: Chen *et al.* [30] map control variables to aerodynamic performance for fast generation, Xie *et al.* [31] link geometric trajectories to flight states for rapid tracking, and Wang *et al.* [32] integrate the A* algorithm with geometric planning for complex no-fly zones. Nevertheless, these methods suffer from poor generalization and limited extensibility.

In contrast, this study proposes a novel trajectory generation methodology for complex, multi-constrained environments that draws from geometric planning while circumventing its limitations. We first design a simple target flight path containing only position information, without specialized geometric designs or manual waypoint tuning. A trajectory tracking algorithm, combined with an iterative stepping strategy and a no-fly zone avoidance strategy, autonomously refines the solution until a feasible trajectory is obtained. The principal contributions are:

- Enhanced computational efficiency and robustness: avoids the convergence difficulties and high cost of direct numerical optimization under complex no-fly zone constraints.
- Intrinsic dynamic feasibility: embeds the vehicle dynamics model within the tracking algorithm, inherently satisfying control and state constraints without post-hoc checks.
- High generalizability and structural simplicity: the simple, automated, iterative framework applies directly to complex no-fly zone configurations without problem-specific modification.

Using a hypersonic morphing vehicle model, our results validate the algorithm and highlight the performance advantages of morphing vehicles over fixed-wing configurations in navigating complex no-fly zones.

*e-mail: flightdc@mail.sysu.edu.cn

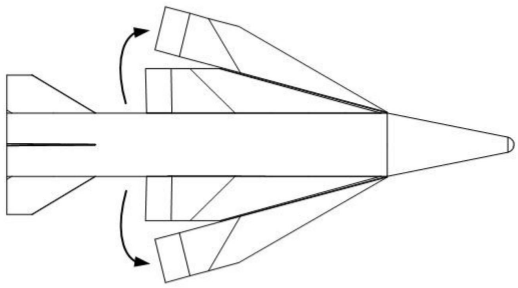

Fig. 1. Vehicle configuration and morphing mechanism.

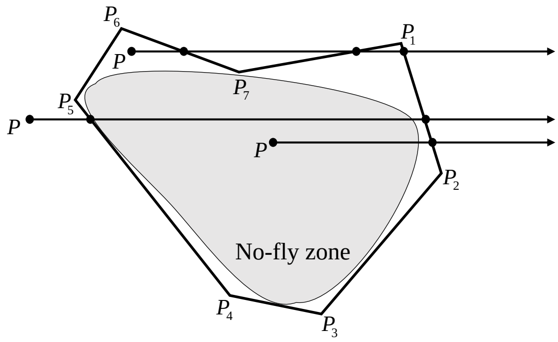

Fig. 2. Polygonal no-fly zone and constraint determination.

Note: In this paper, a path refers to a time-independent sequence of vehicle positions, whereas a trajectory encompasses both position and velocity as functions of time.

2. DYNAMIC MODEL AND CONSTRAINTS

This study focuses on a foldable morphing vehicle, with its configuration detailed in [33] and illustrated in Fig.1. The vehicle features symmetrically and continuously variable wings on both sides. Unlike conventional fixed-wing vehicles, this morphing capability enables dynamic adjustment of three critical aerodynamic parameters—wing area, wingspan, and aspect ratio—thereby altering the aerodynamic forces during flight. The wingspan morphing parameter is defined as $\eta = (b - b_{\min}) / (b_{\max} - b_{\min})$, where b is the current wingspan, and $b_{\min}$ and $b_{\max}$ are the minimum and maximum wingspans, respectively. Clearly, $\eta \in [0, 1]$.

2.1. Dynamics Modeling of Hypersonic Morphing Vehicles

The 3-DOF dynamic model involves the following three coordinate systems: **Geocentric Coordinate System** ($O_E - X_E Y_E Z_E$)**:**, **Launch Coordinate System** ($o - xyz$)**:**, **Velocity Coordinate System** ($o_1 - x_v y_v z_v$)**:** The origin coincides with the vehicle's center of gravity (o_1). The vehicle's center-of-gravity position is described using geocentric longitude, geocentric latitude, and geocentric distance. The dynamic model is established in the velocity coordinate frame. Key attitude parameters—flight path angle, yaw of flight-path angle, and bank angle—are derived from the rotational transformation between the launch and velocity coordinate systems.The definitions of the relevant coordinate systems and Euler angles are provided in reference [34].

The 3-DOF equations of motion for a hypersonic morphing vehicle, neglecting Earth's rotation, engine thrust, and lateral forces (i.e., zero sideslip angle), are:

$$\begin{aligned}
&\dot{v} = -D/m - g\sin\theta \\
&\dot{\theta} = L\cos\nu/mv - g\cos\theta/v + v\cos\theta/r \\
&\dot{\sigma} = L\sin\nu/mv\cos\theta + v\tan\phi\cos\theta\sin\sigma/r \\
&\dot{h} = v\sin\theta \\
&\dot{\lambda} = v\cos\theta\sin\sigma/r\cos\phi \\
&\dot{\phi} = v\cos\theta\cos\sigma/r
\end{aligned} \tag{1}$$

where $[v, \theta, \sigma, h, \lambda, \phi]$ is the flight state vector, comprising velocity, flight path angle, yaw of flight-path angle, altitude, longitude, and latitude. m is the vehicle mass, g is gravitational acceleration, and ν is the bank angle. The geocentric distance is $r = h + R_e$, with R_e denoting Earth's radius. L and D are the aerodynamic lift and drag, given by: $L(D) = 0.5\rho v^2 S C_{L(D)}$, where $\rho = 1.225\mathrm{e}^{-h/h_0}$ is the air density, S is the reference area, and C_L and C_D are the lift and drag coefficients, respectively. Both C_L and C_D depend on the angle of attack α, Mach number Ma, and morphing parameter η, with specific forms provided in the Appendix. The control variables in the trajectory generation model are α, ν, and η.

2.2. Problem Constraints

The following path constraints, control constraints, and no-fly zone constraints are considered. The vehicle is subject to several path constraints, including conventional limits on heating rate $\dot{Q}$, dynamic pressure q, and total load factor n. Control constraints are also essential, encompassing limits on the angle of attack α, bank angle ν, and morphing parameter η. The models for these path and control constraints are referenced from [22].

Traditional circular no-fly zone models are simple and easily integrated with trajectory generation algorithms. However, real no-fly zones often have complex shapes, and approximating them with circles may include large feasible regions within the boundary, thus reducing the effectiveness of trajectory generation. To address this, we propose a polygonal modeling approach: multiple feature points are selected along the edge of the no-fly zone and connected sequentially to form an enclosing polygon, as shown in Fig.2. This polygon accurately captures the complex shape of the actual no-fly zone while maintaining a relatively simple structure for trajectory generation analysis. Determining whether the vehicle lies inside a circular no-fly zone simply requires calculating the distance to its center; polygonal no-fly zones present a more complex challenge. We therefore employ the ray casting method for point-in-polygon determination [35], as illustrated in Fig.2.

This method draws a horizontal ray from the current vehicle position P and counts its intersections with the polygon edges. If the intersection count is odd, the vehicle is inside the no-fly zone; if even, it is outside. The ray casting method offers a straightforward means of determining vehicle location relative to a polygonal no-fly zone. The key lies in determining whether the ray intersects each polygon edge. Given two vertices of an edge, $P_1(x_1, y_1)$ and $P_2(x_2, y_2)$, and the current point $P_0(x_0, y_0)$, the horizontal coordinate of the intersection between a rightward horizontal ray through P_0 and the line through P_1 and P_2 is:

$$x = (y_0 - y_1)(x_1 - x_2)/(y_1 - y_2) + x_1 \tag{2}$$

The ray is directed horizontally to the right. An intersection with that edge is confirmed when:

$$\begin{cases} x > x_0 \\ x \in (x_1, x_2) \end{cases} \tag{3}$$

Otherwise, no intersection exists.

Three special cases require separate handling: 1) **Vertex intersection**: When the ray passes through a polygon vertex (left panel of Fig.3), the intersection is counted only once. 2) **Vertex-edge intersection**: If the ray intersects both a vertex and an edge (middle panel of Fig.3), that intersection is disregarded. 3) **Edge coincidence**: When the ray coincides with a polygon edge (right panel of Fig.3), that edge is excluded from the intersection count.

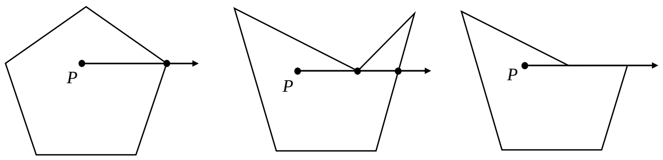

Fig. 3. Special cases where rays intersect the polygonal no-fly zone.

3. TRAJECTORY GENERATION FOR HYPERSONIC MORPHING VEHICLES WITH NO-FLY ZONE CONSTRAINTS

This paper presents an approach to designing a flight path that satisfies multiple irregular no-fly zone constraints. The flight path is first discretized, and an optimization problem is formulated to minimize the distance between the vehicle's terminal position and the target point within each discrete interval. A trajectory generation algorithm then computes a feasible trajectory that satisfies all vehicle constraints.

3.1. Target Flight Path Design

To handle multiple irregular no-fly zones, a polynomial interpolation method is employed for its simplicity and smoothness. Key points in the flight domain are first selected based on the no-fly zone locations, as shown in Fig.4.

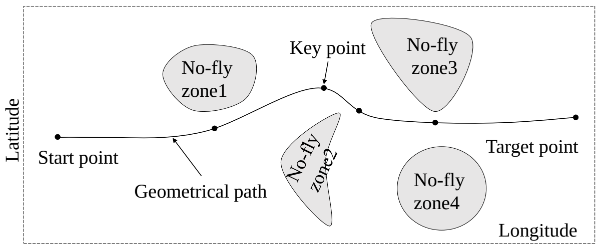

Fig. 4. Horizontal target flight path design for no-fly zone constraints.

Polynomial interpolation using the key points, start point, and target point yields the vehicle target flight path:

$$\phi = \sum_{i=0}^{n} a_i \lambda^i \tag{4}$$

where a_i are the polynomial coefficients. The flight path tangent at the start point must align with the vehicle's velocity direction, thus satisfying:

$$\frac{\mathrm{d}\phi}{\mathrm{d}\lambda}\Big|_{\lambda=\lambda_0} = \frac{v_\phi}{v_\lambda}\Big|_{\lambda=\lambda_0} \tag{5}$$

The 3D path also incorporates altitude. Following the traditional atmospheric re-entry profile design, the vehicle initially descends rapidly to trade altitude for speed, then transitions into a quasi-equilibrium glide mode with gradual altitude changes.

The vertical flight path is subject to constraints analogous to Eq.5, which are omitted here. Combining the latitude and altitude polynomials with longitude yields the target flight path satisfying no-fly zone constraints. Notably, this path contains only position information, excluding velocity and time.

3.2. Flight Trajectory Generation Method

The flight trajectory must satisfy both no-fly zone and vehicle-specific constraints. While the designed flight path meets the former, it lacks velocity and time information, making it impossible to verify path constraints, dynamics, and control constraints. Our objective is to design a trajectory incorporating both position and velocity information, thereby ensuring feasibility. The core challenge lies in solving time-dependent control variables. To reduce complexity, we discretize the target flight path and solve the control variables for each segment separately.

3.2.1. Flight Path Discretization A smaller discretization step more accurately characterizes the original flight path but reduces computational efficiency, while a larger step improves efficiency at the cost of accuracy. Large path variations require small steps; small variations (e.g., straight lines) permit larger steps. The path variation is quantified by the radius of curvature. To balance efficiency and accuracy, the discretization step d_i is calculated based on the local radius of curvature R_i:

$$d_i = \begin{cases} k_R R_i & R_i \le R^{\max} \\ d^{\max} & R_i > R^{\max} \end{cases} \tag{6}$$

where $R^{\max}$ is the upper limit of the radius of curvature, $d^{\max}$ is the upper limit of the discrete step, and k_R is the discrete step factor. The velocities of adjacent discrete intervals must satisfy continuity, i.e., $v_{end}^{i} = v_{start}^{i+1}$, with the initial velocity given by $v_{start}^{1} = v_{start}$.

3.2.2. Control Variable Calculation To enhance efficiency, we approximate the control variables as constant within each discrete interval, given their negligible variation. Using Eq.1 and treating the initial position and velocity as known, the terminal state is expressed as:

$$x^f = f(\alpha, v, \eta, t) \tag{7}$$

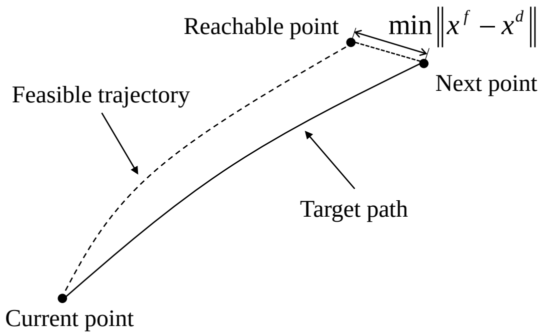

Fig. 5. Target path and feasible trajectory.

As shown in Fig.5, x^d is the target position, x^f is the reachable position, and $u = [\alpha, \nu, \eta, t]$ serves as the optimization variable for the following problem:

Optimization objective:

$$\min \quad \left\| x^f - x^d \right\| \tag{8}$$

Dynamic model constraints (from Eq.1):

$$\dot{x} = f(x, u) \tag{9}$$

together with the path and control constraints in Section 2.2.

Since the optimization variables $[\alpha, \nu, \eta, t]$ are constant, the computational cost is small, and the problem can be solved using a conventional nonlinear programming solver.

3.2.3. Iterative Stepping Strategy Directly selecting the next discrete point as the target after each computation cycle may cause divergence by ignoring the vehicle's limited maneuverability. Proper target point selection is thus crucial. This paper proposes a selection method based on the relative position of the reachable point to the current target point, as illustrated in Fig.6:

1. Determine the flight direction $\vec{r}_1$ from the current point to the target point;
2. Calculate the reachable point using the control variables and time from Section 3.2.2;
3. Determine the direction $\vec{r}_2$ from the target point to the reachable point;
4. Calculate the cosine of the angle between the two vectors.

The target point selection criterion is:

1. If $\cos\theta < 0$, retain the current target point for the next cycle.
2. If $\cos\theta \geq 0$, select the next discrete point as the target point.

3.2.4. No-Fly Zone Avoidance Strategy Due to limited maneuverability, the reachable point may enter the no-fly zone, especially near its boundary. To address this, a no-fly zone avoidance strategy offsets the target point perpendicularly away from the no-fly zone boundary, as shown in Fig.7.

When the reachable point lies within the no-fly zone, the target point is adjusted away from it. This modifies the optimization objective and guides the vehicle away from the no-fly zone. The adjusted target point $x^{d'}$ is computed as:

$$x^{d'} = x^d + k_p \left(x^d - x^f \right) \tag{10}$$

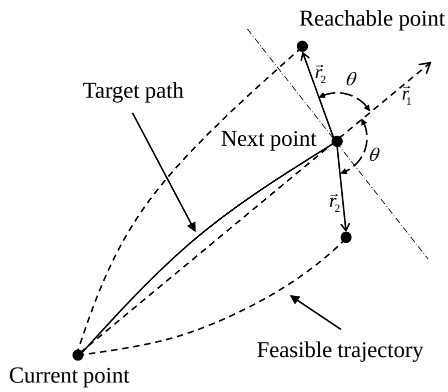

Fig. 6. Iterative stepping strategy.

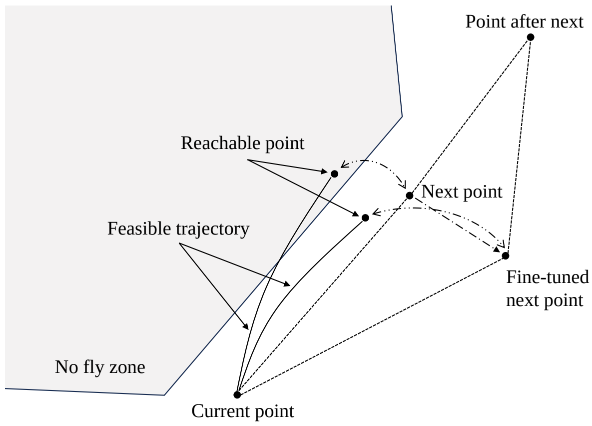

Fig. 7. No-fly zone avoidance strategy.

where k_p is the amplification factor.

3.3. Algorithm Design

Combining the above components, the trajectory generation algorithm is summarized in Fig.8. The main steps are:

1. Select key points in the flight domain based on no-fly zone constraints and the initial position. Construct and discretize the target path.
2. Formulate the optimization problem with control variables and flight time as variables, minimizing the distance between reachable and target positions subject to vehicle constraints.
3. Select an appropriate target position using the iterative stepping strategy.
4. Solve the optimization model to obtain the optimal control variables, flight time, and reachable position.
5. If the reachable point lies within the no-fly zone, apply the no-fly zone avoidance strategy (offset the target point away from the zone) and return to step 4; otherwise, proceed.
6. If the termination condition is not met, set the terminal position and velocity as the new initial state and return to step 3; otherwise, proceed.
7. Output the control strategy and the feasible trajectory satisfying all constraints.

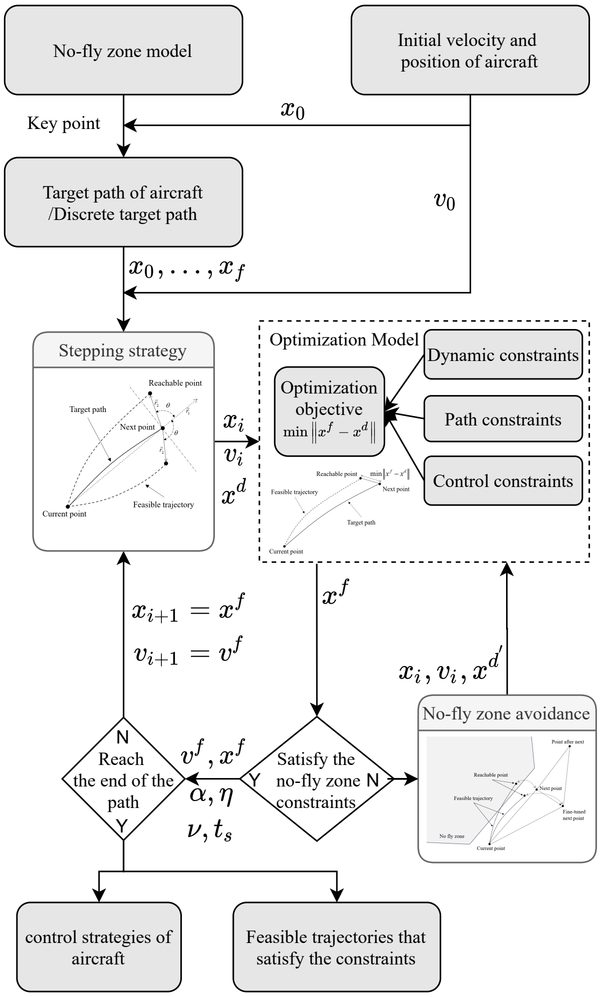

Fig. 8. Trajectory generation process under complex no-fly zone constraints.

Table 1. Control variable constraints and path constraints.

Parameters	Min	Max	Units
Angle of attack α	-10	30	deg
Bank angle ν	-60	60	deg
Morphing parameter η	0.1	1	–
Heating rate $\dot{Q}$	–	3000	$\mathrm{kW/m^2}$
Dynamic pressure q	–	100	kPa
Total load factor n	–	6	–

4. NUMERICAL SIMULATIONS

The trajectory optimization problem under no-fly zone constraints is investigated using the hypersonic morphing vehicle model. Control variable constraints and path constraints are listed in Table 1, initial flight conditions in Table 2, and the vertex coordinates of three irregular polygonal no-fly zones in Table 3. The no-fly zone altitude ranges from 0 to 100 km, covering the vehicle's entire flight airspace.

Table 2. Initial flight conditions.

Parameters	Value	Units
Velocity v	15	Ma
Flight path angle θ	0	deg
Yaw of flight-path angle σ	90	deg
Altitude h	80	km
Longitude λ	0	deg
Latitude ϕ	0	deg

Table 3. Vertex coordinates of the polygonal no-fly zones.

No-fly zone 1		No-fly zone 2		No-fly zone 3	
λ	ϕ	λ	ϕ	λ	ϕ
13	-0.2	16	-0.8	25	2.5
16	0.0	18	-2.0	20	0.8
14	1.5	24	-2.5	26	1.5
10	1.0	25	-1.2	30	1.0
11	0.0	25	0.1	–	–
–	–	22	0.2	–	–

4.1. Reachable Domain Analysis under No-Fly Zone Constraints

Compared to fixed-wing vehicles, hypersonic morphing vehicles possess an additional control variable, enabling enhanced maneuverability. This is reflected in the expanded feasible intervals of acceleration, flight path angle rate, and yaw of flight-path angle rate, as shown in Fig.9, derived from the dynamic model and aerodynamic parameters in Section 2.2. The dark shaded region represents the feasible interval for fixed-wing vehicles at $\eta = 0.5$, while the light shaded region denotes that for morphing vehicles over $\eta \in [0.1, 1.0]$. The light regions envelop the dark ones, confirming the larger feasible regions and superior maneuverability of morphing vehicles.

To further illustrate this advantage, a reachable domain analysis for a conventional circular no-fly zone is conducted using both vehicle models. The terminal constraint is:

$$\begin{aligned} \phi^{end} &= 0 \\ \lambda^{end} &> 6 \end{aligned} \tag{11}$$

with minimizing λ^{end} as the objective. The resulting reachable domains are shown in Fig.10.

The dark shaded region represents the unreachable domain of the morphing vehicle, while the light shaded region denotes that of the fixed-wing vehicle. The light region contains the dark region, confirming that the morphing vehicle has a larger reachable domain behind the no-fly zone and thus superior maneuverability.

4.2. Trajectory Generation under Complex No-Fly Zone Constraints

4.2.1. Target Flight Path Design Based on the irregular no-fly zones in Table 3, the selected key points and polynomial coefficients for the $\lambda - \phi$ plane are listed in Tables 4 and 5; those for the $\lambda - h$ plane appear in Tables 6 and 7. The resulting 3D target flight path satisfies the no-fly zone constraints.

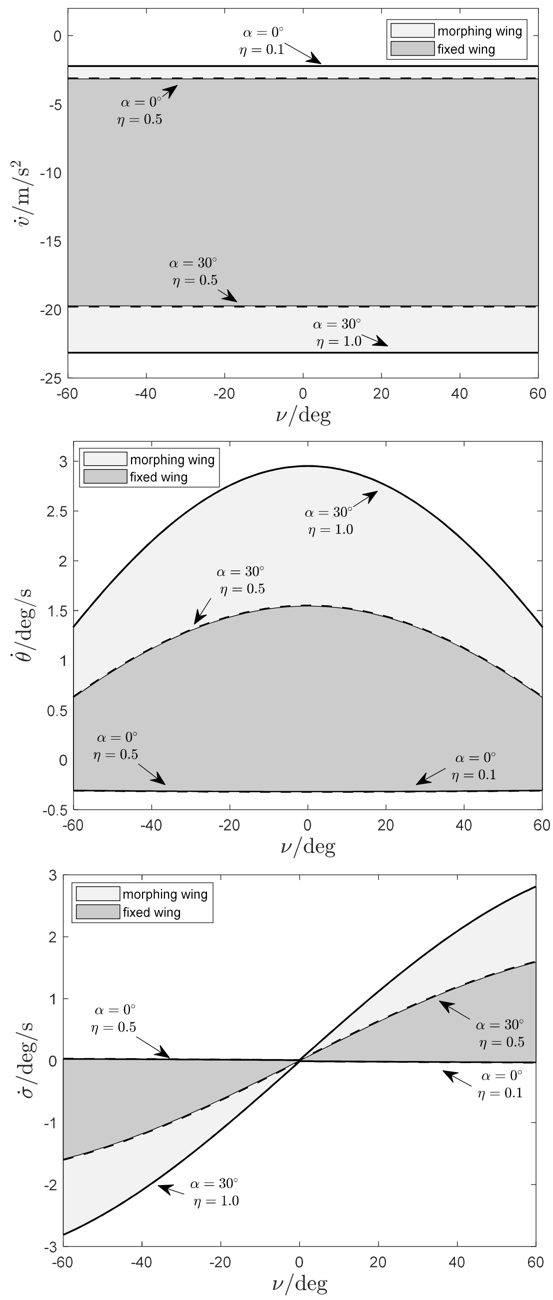

Fig. 9. Acceleration, flight path angle rate, and yaw of flight-path angle rate of morphing and fixed-wing vehicles.

Table 4. Key points in the $\lambda - \phi$ plane.

	P1	P2	P3	P4	P5	P6
λ (deg)	5	10	15	20	25	30
ϕ (deg)	-0.1	-0.2	-0.5	0.3	1	0

Table 5. Polynomial coefficients of the flight path in the $\lambda - \phi$ plane.

Coefficient	a_0	a_1	a_2	a_3
Value	0	0	-0.0564	0.0227
a_4	a_5	a_6	a_7	a_8
-0.0035	2.65e-4	-1.02e-5	1.94e-7	-1.45e-9

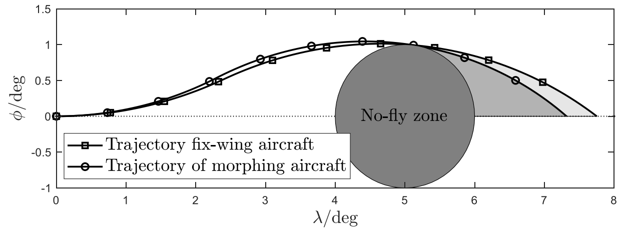

Fig. 10. Reachable domains under no-fly zone constraints for morphing and fixed-wing vehicles.

Table 6. Key points in the $\lambda - h$ plane.

	P1	P2	P3	P4
λ (deg)	0	10	22	35
h (km)	80	40	50	20

Table 7. Polynomial coefficients of the flight path in the $\lambda - h$ plane.

a_0	a_1	a_2	a_3	a_4	a_5
80	-5.885e-11	-1.298	0.1286	-0.00437	4.9e-05

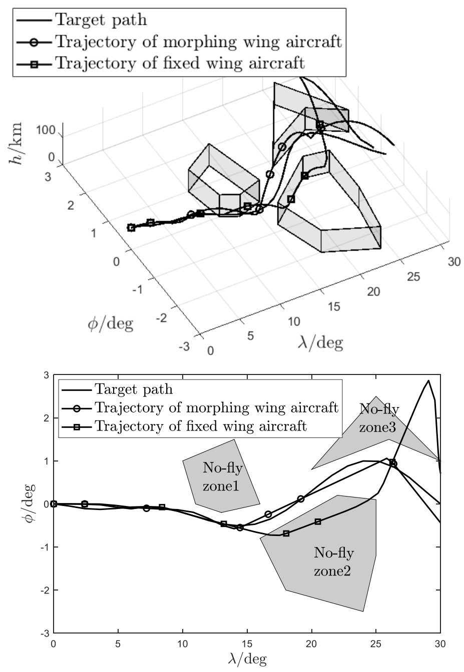

Fig. 11. Optimized trajectories under complex no-fly zone constraints.

4.2.2. Trajectory Generation The simulation was developed in MATLAB R2018a using the `fmincon` solver (interior-point algorithm). With $k_p = 0.5$, $\eta \in [0.1, 1.0]$ for the morphing vehicle, and $\eta = 0.8$ for the fixed-wing vehicle, the feasible trajectories are shown in Fig.11. The morphing vehicle successfully satisfies the no-fly zone constraints, whereas the fixed-wing vehicle's trajectory intersects a no-fly zone. Even with the avoidance strategy in Section 3.2.4, the fixed-wing vehicle's limited flight capability prevents the optimization algorithm from placing the reachable point outside the no-fly zone.

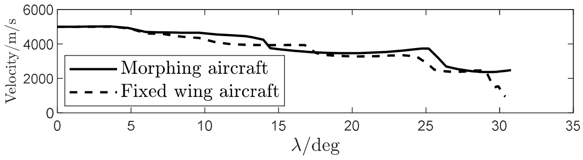

Fig. 12. Velocity profiles of the two vehicles.

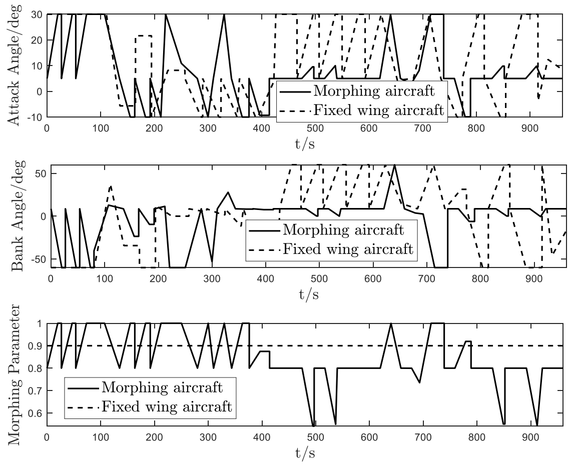

Fig. 13. Control variable profiles of the two vehicles.

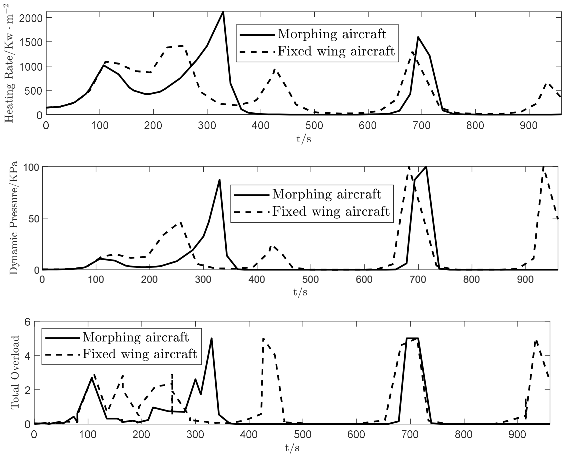

Fig. 14. Path constraint profiles of the two vehicles.

Velocity profiles in Fig.12 show that the morphing vehicle's terminal velocity exceeds 2000 m/s, retaining significant maneuvering potential, while the fixed-wing vehicle consumes substantial energy during wide-range avoidance maneuvers, causing a drastic terminal velocity drop.

Control variable profiles in Fig.13 confirm that both vehicles satisfy control constraints, with reasonable bank angle reversals, validating the algorithm's practicality. The morphing vehicle exhibits smaller frequency and amplitude of bank angle and angle of attack variations, highlighting its control advantages. Path constraint profiles in Fig.14 show that both vehicles satisfy all path constraints throughout flight.

These results demonstrate that the proposed algorithm generates feasible trajectories under complex no-fly zone configurations with a simple and generalizable structure. The morphing vehicle exhibits stronger maneuvering capability and outperforms the fixed-wing vehicle in responding to complex no-fly zone constraints.

4.2.3. Statistical Results To further validate the algorithm, nine test cases with one to four polygonal no-fly zones were randomly generated using the same dynamics model and initial conditions. The resulting trajectories are shown in Fig.15.

Across all nine cases, the morphing vehicle's trajectories satisfy all no-fly zone constraints, whereas the fixed-wing vehicle fails in the sixth case. These results further demonstrate the morphing vehicle's enhanced flight capability and the algorithm's effectiveness under multiple complex no-fly zone constraints.

4.2.4. Baseline Comparison A comparative study was conducted using the pseudo-spectral method under identical complex no-fly zone constraints. As shown in Fig.16, a triangular no-fly zone was designed. The pseudo-spectral method requires constructing a circular containment region enclosing the no-fly zone, which significantly exceeds the original triangular zone and reduces the feasible solution space.

Using bank angle as the control variable with identical dynamics and initial conditions, both methods were applied. The resulting trajectories appear in Fig.16.

Both methods satisfy the no-fly zone constraints. However, due to the larger circular no-fly zone required by the pseudo-spectral method, the proposed approach achieves a significantly shorter path length. Figure 17 compares the bank angle profiles.

The pseudo-spectral method requires aggressive control variations, whereas the proposed approach accomplishes avoidance with significantly fewer bank angle reversals, substantially reducing the control system burden.

5. DISCUSSION

The polynomial construction method for initial path planning requires predefined key points based on no-fly zone features, which currently lacks automation, limiting practicality. In low-speed UAV trajectory planning, numerous optimization algorithms have been developed for feasible path generation. Since our initial path design considers only no-fly zone constraints without vehicle path constraints, these UAV algorithms remain applicable. We implement four algorithms—Artificial Potential Field (APF), A-star, Dynamic Window Approach (DWA), and RRT-star—to generate initial target paths, as shown in Fig.18.

These algorithms have distinct characteristics:

1. **A-star**: A heuristic search algorithm that quickly finds the shortest path, but consumes substantial computational resources and exhibits low efficiency under complex no-fly zone constraints.
2. **RRT-star**: Expands a tree structure and optimizes the path by directing sampled points toward the target. It generates feasible paths quickly, offering speed advantages.

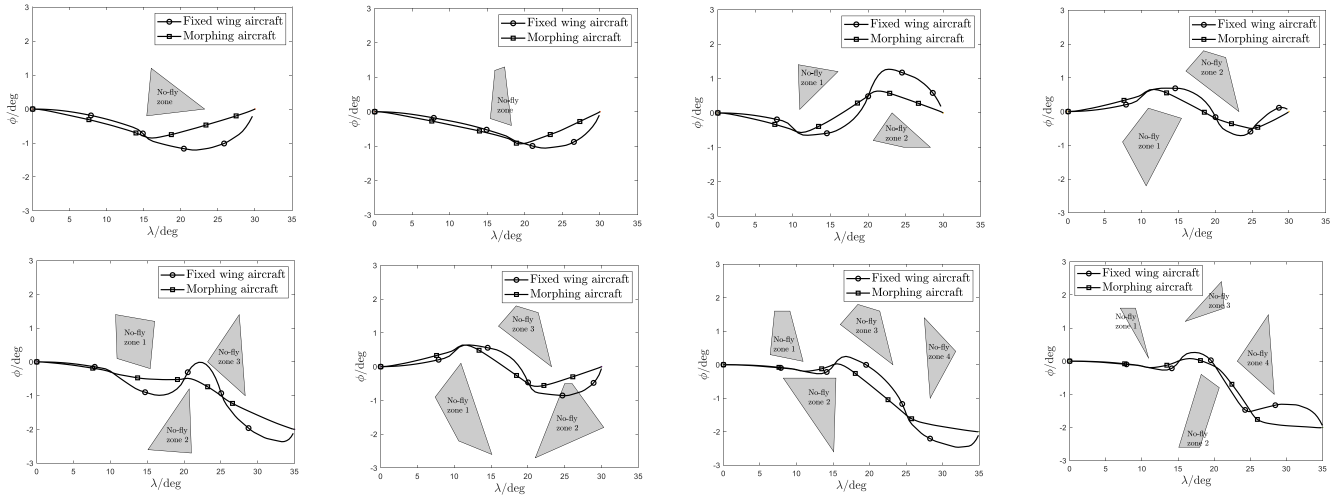

Fig. 15. Comparative study of trajectory generation in randomly generated complex no-fly zones.

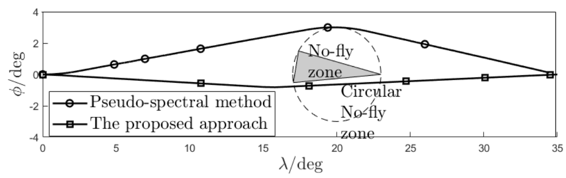

Fig. 16. Comparative analysis with the pseudo-spectral method.

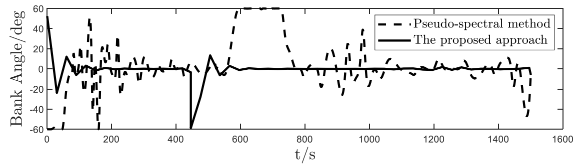

Fig. 17. Bank angle profiles: comparative analysis.

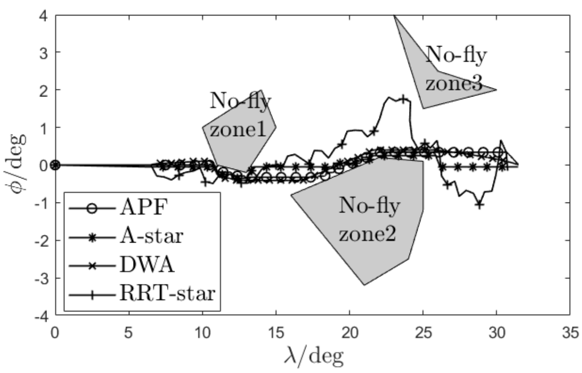

Fig. 18. Initial flight paths designed by typical path planning algorithms.

3. **APF**: Features simple structure and ease of implementation, generating smooth paths, but is prone to local optima and requires careful coefficient design.
4. **DWA**: Offers high computational efficiency and simple implementation, suitable for resource-limited systems, but is susceptible to local optima.

A comparative evaluation of these four algorithms based on computational efficiency, space complexity, and deterministic behavior is presented in Table 8.

Table 8. Comparative performance analysis of heuristic path planners.

Algorithm	A-star	RRT-star	APF	DWA
Time (s)	1.2	3.8	0.4	0.8
Space complexity	High	Medium	Low	Low
Key advantage	Globally optimal; deterministic	Handles high-dim. constraints; asymptotically optimal	Real-time reactive; smooth path	Considers velocity; acceleration
Key limitation	Dense, zigzag waypoints; memory intensive	Stochastic; needs heavy pruning	Local minima near concave obstacles	Short-sighted; poor global detour

To bridge the gap between the geometric reference path and the sparse parameterization required for trajectory optimization, we adopt a curvature-driven adaptive resampling criterion: sharper turns receive denser waypoints; straighter segments, sparser sampling.

Given an initial reference path of discrete waypoints, the local turning angle θ_i at each point P_i is:

$$\theta_i = \arccos\left(\frac{\vec{v}_{i-1}\cdot\vec{v}_i}{|\vec{v}_{i-1}||\vec{v}_i|}\right) \tag{12}$$

where $\vec{v}_{i-1} = P_i - P_{i-1}$ and $\vec{v}_i = P_{i+1} - P_i$. Key points are extracted as follows: retain P_i if $\theta_i > \theta_{\text{threshold}}$ (significant turn); remove P_i if $\theta_i \le \theta_{\text{threshold}}$ and the accumulated arc-length since the last retained point does not exceed $L_{\max}$. This two-parameter scheme ($\theta_{\text{threshold}}$ and $L_{\max}$) captures the essential geometric features of the avoidance path while eliminating redundant nodes along straight corridors.

For different application scenarios, combining or selecting algorithms based on their respective advantages can enable faster and more effective initial path planning for constrained vehicles, thereby achieving automation in initial flight path design.

6. CONCLUSION

This paper presents a trajectory generation algorithm for complex no-fly zone avoidance. By integrating the hypersonic morphing vehicle dynamic model, we achieved trajectory generation under complex no-fly zone constraints and compared the results with those of a fixed-wing vehicle. The primary contributions are:

1. A trajectory generation algorithm with simple structure and strong generality was designed to address the poor convergence of existing methods under complex no-fly zone constraints, achieved through suitable stepping strategies, no-fly zone avoidance strategies, and optimization models.
2. Using the proposed algorithm, trajectories were generated for both hypersonic morphing and fixed-wing vehicles under complex no-fly zone constraints. Simulation results highlight the morphing vehicle's advantages in reachable domain and avoidance capability.

The simulations validate the algorithm's effectiveness and demonstrate that hypersonic morphing vehicles possess stronger maneuverability and superior flight performance compared to fixed-wing vehicles. Future work will extend the algorithm to moving targets and dynamic environments. Target mobility will increase computational load and reduce real-time performance, as the current method relies on no-fly zone-based reference trajectory calculation. Therefore, future improvements will focus on optimizing algorithmic efficiency and increasing computational speed to enable practical real-time trajectory generation.

APPENDIX

Aerodynamic coefficient modeling:

$$\begin{aligned} C_L &= C_{L_0} + C_{L\alpha}\alpha + C_{L\alpha^2}\alpha^2 + C_{LMa}Ma + C_{L\alpha Ma}\alpha Ma \\ C_D &= C_{D_0} + C_{D\alpha}\alpha + C_{D\alpha^2}\alpha^2 + C_{DMa}Ma + C_{D\alpha Ma}\alpha Ma \end{aligned} \tag{13}$$

Aerodynamic derivative:

$$\begin{aligned} \begin{bmatrix} C_{L_0} \\ C_{L\alpha} \\ C_{L\alpha^2} \\ C_{LMa} \\ C_{L\alpha Ma} \end{bmatrix} &= \begin{bmatrix} 0.3015 & -0.3018 & 0.0090 \\ -9.7555 & 24.0689 & -2.1968 \\ 8.1804 & -9.4726 & 2.4020 \\ -0.0326 & 0.0360 & -0.0059 \\ 0.2953 & -0.7559 & 0.1098 \end{bmatrix} \begin{bmatrix} \eta^2 \\ \eta \\ 1 \end{bmatrix} \\ \begin{bmatrix} C_{D_0} \\ C_{D\alpha} \\ C_{D\alpha^2} \\ C_{DMa} \\ C_{D\alpha Ma} \end{bmatrix} &= \begin{bmatrix} -0.0428 & 0.1935 & 0.1243 \\ 0.0356 & 0.1543 & 0.0029 \\ -2.3049 & 4.1167 & 1.7399 \\ 0.0058 & -0.0112 & -0.0024 \\ 0.0003 & -0.0127 & -0.0039 \end{bmatrix} \begin{bmatrix} \eta^2 \\ \eta \\ 1 \end{bmatrix} \end{aligned} \tag{14}$$

ACKNOWLEDGEMENTS

This work was supported by Shenzhen Science and Technology Program (No.: JCYJ20250604175546060).

REFERENCES

[1] Q. Ma, Y. Yin, and X. Shi, "Review of research methods for hypersonic vehicle reentry trajectory planning," *Frontiers in Computing and Intelligent Systems*, vol. 2, no. 1, pp. 142–145, 2022, doi: 10.54097/fcis.v2i1.3343.

[2] R. Chai, A. Savvaris, A. Tsourdos, S. Chai, and Y. Xia, "A review of optimization techniques in spacecraft flight trajectory design," *Progress in aerospace sciences*, vol. 109, p. 100543, 2019, doi: 10.1016/j.paerosci.2019.05.003.

[3] H. Jiao, X. Zhang, T. Xu, and W. Fu, "Trajectory optimization method of hypersonic vehicle based on pso-gpm," in *International Conference on Autonomous Unmanned Systems*. Springer, 2024, pp. 295–305.

[4] S. Ma, Y. Yang, H. Yang, and W. Chen, "Trajectory optimization of hypersonic vehicle considering the quasi-static assumption of pitch motion," *Aerospace Science and Technology*, vol. 146, p. 108969, 2024, doi: 10.1016/j.ast.2024.108969.

[5] Y. Luo, J. Wang, J. Jiang, and H. Liang, "Reentry trajectory planning for hypersonic vehicles via an improved sequential convex programming method," *Aerospace Science and Technology*, vol. 149, p. 109130, 2024.

[6] D.-m. Liu, J.-s. Cui, W. Wang, M.-h. Wang, C.-h. Wang, and S.-p. Zhou, "A convex trajectory planning method for the dive phase of hypersonic vehicles with multiple constraints," *Proceedings of the Institution of Mechanical Engineers, Part G: Journal of Aerospace Engineering*, p. 09544100251406754, 2025.

[7] Y. Tao, Z. Li, K. Liu, and W. Huang, "Research on the application of artificial intelligence in the trajectory of hypersonic flight aircraft," in *2025 IEEE 10th International Conference on Data Science in Cyberspace (DSC)*. IEEE, 2025, pp. 423–430.

[8] S. Srithar, E. Vetrimani, K. P. Reddy, S. Kodati, and S. Alagumuthukrishnan, "Artificial hyperintelligence-enabled cyber-physical system control for autonomous vehicles," *Smart Grids as Cyber Physical Systems: Artificial Intelligence, Cybersecurity, and Clean Energy for Next Generation Smart Grids*, vol. 1, pp. 145–162, 2024.

[9] V. R. Makkapati, J. Ridderhof, P. Tsiotras, J. Hart, and B. van Bloemen Waanders, "Desensitized trajectory optimization for hypersonic vehicles," in *2021 IEEE Aerospace Conference (50100)*. IEEE, 2021, pp. 1–10, doi: 10.1109/aero50100.2021.9438511.

[10] B. Yang, L. Wang, and J. Fu, "Improved snake optimization algorithm for parameter identification based on the genetic algorithm," *Bulletin of the Polish Academy of Sciences Technical Sciences*, vol. 74, no. 1, p. e156797, 2026.

[11] S. Liu, S. Liu, B. Yan, T. Zhang, X. Zhang, and J. Yan, "Interception of a hypersonic vehicle by low-

speed interceptors: novel perspectives and cost optimisation," *Bulletin of the Polish Academy of Sciences. Technical Sciences*, vol. 70, no. 6, 2022, doi: 10.24425/bpasts.2022.143537.

[12] E. S. Rudnick-Cohen, G. W. Reich, A. M. Pankonien, and P. S. Beran, "Robust optimal design and trajectory planning of an aircraft with morphing airfoil sections," *Structural and Multidisciplinary Optimization*, vol. 66, no. 10, p. 214, 2023, doi: 10.1007/s00158-023-03664-z.

[13] E. S. Rudnick-Cohen, J. D. Hodson, G. W. Reich, A. M. Pankonien, and P. S. Beran, "Design and trajectory planning optimization of a morphing airfoil for 3-d flight maneuvers," in *AIAA Scitech 2021 Forum*, 2021, p. 0890, doi: 10.2514/6.2021-0890.

[14] G. Cai, J. Qin, K. Luo, and Z. Liu, "Online trajectory planning of morphing vehicle based on sequential convex programming," in *Asia-Pacific International Symposium on Aerospace Technology*. Springer, 2023, pp. 727–737, doi: 10.1007/978-981-97-4010-$9_5$5.

[15] H. Wang, C. Yu, and X. Cheng, "Trajectory planning of morphing aircraft based on the probability of passing through threat zones," *Aerospace control*, vol. 42, no. 2, pp. 35–41, 2024, doi: 10.1109/ispcem64498.2024.00124,in Chinese.

[16] S.-D. Lee, C.-H. Lee, and S.-Y. Kim, "Pseudospectral convex optimization for reentry vehicle guidance with no-fly zone constraints," in *Asia-Pacific International Symposium on Aerospace Technology*. Springer, 2021, pp. 179–197, doi: 10.1007/978-981-19-2635-$8_1$4.

[17] L. Qu, P. Wang, and H. He, "Research on trajectory planning method for variable sweep back aircraft with no fly zone margin," *Advances in Engineering Technology Research*, vol. 10, no. 1, pp. 276–276, 2024, doi: 10.56028/aetr.10.1.276.2024.

[18] K. Heo, G. Park, and K. Lee, "On correcting errors in existing mathematical approaches for uav trajectory design considering no-fly-zones," *arXiv preprint arXiv:2308.13001*, 2023, doi: 10.1109/ucom59132.2023.10257652.

[19] K. Heo, G. Park, and K. Lee, "Joint optimization of uav trajectory and communication resources with complete avoidance of no-fly-zones," *IEEE Transactions on Intelligent Transportation Systems*, vol. 25, no. 10, pp. 14 259–14 265, 2024.

[20] X. Xu, J. Song, K. Zhao, X. Tong, and Y. Zhang, "Real-time trajectory planning for hypersonic vehicle with dynamic no-fly zone constraints," in *International Conference on Guidance, Navigation and Control*. Springer, 2022, pp. 3317–3326, doi: 10.1007/978-981-19-6613-$2_3$22.

[21] M. He and Y. Nan, "A composite planning method considering avoidance of multiple no-fly zones," in *Journal of Physics: Conference Series*, vol. 2764, no. 1. IOP Publishing, 2024, p. 012054, doi: 10.1088/1742-6596/2764/1/012054.

[22] R.-z. He, L.-h. Liu, G.-j. Tang, and W.-m. Bao, "Rapid generation of entry trajectory with multiple no-fly zone constraints," *Advances in Space Research*, vol. 60, no. 7, pp. 1430–1442, 2017, doi: 10.1016/j.asr.2017.06.046.

[23] Y. Zhang, R. Zhang, and H. Li, "Graph-based path decision modeling for hypersonic vehicles with no-fly zone constraints," *Aerospace Science and Technology*, vol. 116, p. 106857, 2021, doi: 10.1016/j.ast.2021.106857.

[24] Y. Zhang, R. Zhang, and H. Li, "Mixed-integer trajectory optimization with no-fly zone constraints for a hypersonic vehicle," *Acta Astronautica*, vol. 207, pp. 331–339, 2023, doi: 10.1016/j.actaastro.2023.03.031.

[25] P. Vernis and E. Ferreira, "On-board trajectory planner for the taem guidance of a winged-body," *EADS Space Transportation*, vol. 9, 2005, doi: 10.2514/6.1997-3555.

[26] P. Joyce, J. Pomroy, and L. Grindle, "The hyper-x launch vehicle: challenges and design considerations for hypersonic flight testing," Master's thesis, 2005.

[27] T. R. Jorris and R. G. Cobb, "Three-dimensional trajectory optimization satisfying waypoint and no-fly zone constraints," *Journal of Guidance, Control, and Dynamics*, vol. 32, no. 2, pp. 551–572, 2009, doi: 10.2514/1.37030.

[28] T. R. Jorris and R. G. Cobb, "Multiple method 2-d trajectory optimization satisfying waypoints and no-fly zone constraints," *Journal of Guidance, Control, and Dynamics*, vol. 31, no. 3, pp. 543–553, 2008, doi: 10.2514/1.32354.

[29] R. Sáez, H. Khaledian, X. Prats, A. Guitart, D. Delahaye, and E. Feron, "A fast and flexible emergency trajectory generator enhancing emergency geometric planning with aircraft dynamics," 2021.

[30] X. Chen, C. Li, C. Gong, L. Gu, and D. R. Andrea, "A study of morphing aircraft on morphing rules along trajectory," *Chinese Journal of Aeronautics*, vol. 34, no. 7, pp. 232–243, 2021, doi: 10.1016/j.cja.2020.04.032.

[31] Y. Xie, S. Peng, Y. Zhang, H. Zhu, J. Cheng, and Y. Li, "Rapid adaptive planning of glide trajectory based on inverse dynamics," in *2023 China Automation Congress (CAC)*. IEEE, 2023, pp. 8541–8546, doi: 10.1109/cac59555.2023.10450773.

[32] L. Wang, H. Liu, D. Yang, J. Liu, Z. Qi, and X. Yue, "A method for real-time planning of hypersonic cruise trajectory," in *Advances in Guidance, Navigation and Control: Proceedings of 2020 International Conference on Guidance, Navigation and Control, ICGNC 2020, Tianjin, China, October 23–25, 2020*. Springer, 2022, pp. 3963–3973, doi: 10.1007/978-981-15-8155-$7_3$31.

[33] W. Peng, T. Yang, Z. Feng, and Q. Zhang, "Analysis of morphing modes of hypersonic morphing aircraft and multiobjective trajectory optimization," *IEEE Access*, vol. 7, pp. 2244–2255, 2018, doi: 10.1109/access.2018.2886252.

[34] P. H. Zipfel, *Modeling and simulation of aerospace vehicle dynamics*. Aiaa, 2000.

[35] M. El-Salamony and A. Guaily, "Enhanced modified-polygon method for point-in-polygon problem," pp. 47–61, 2020.